PAPER

Structural investigations of Au–Ni aerogels: morphology and element distribution†

Johannes Kresse,[a] Maximilian Georgi,[a] René Hübner [iD][b] and Alexander Eychmüller [iD] *[a]

The physical properties of nanomaterials are determined by their structural features, making accurate structural control indispensable. This carries over to future applications. In the case of metal aerogels, highly porous networks of aggregated metal nanoparticles, such precise tuning is still largely pending. Although recent improvements in controlling synthesis parameters like electrolytes, reductants, or mechanical stirring, the focus has always been on one particular morphology at a time. Meanwhile, complex factors, such as morphology and element distributions, are studied rather sparsely. We demonstrate the capabilities of precise morphology design by deploying Au–Ni, a novel element combination for metal aerogels in itself, as a model system to combine common aerogel morphologies under one system for the first time. Au–Ni aerogels were synthesized *via* modified one- and two-step gelation, partially combined with galvanic replacement, to obtain aerogels with alloyed, heterostructural (novel metal aerogel structure of interconnected nanoparticles and nanochains), and hollow spherical building blocks. These differences in morphology are directly reflected in the physisorption behavior, linking the isotherm shape and pore size distribution to the structural features of the aerogels, including a broad-ranging specific surface area (35–65 m^2 g^{-1}). The aerogels were optimized regarding metal concentration, destabilization, and composition, revealing some delicate structural trends regarding the ligament size and hollow sphere character. Hence, this work significantly improves the structural tailoring of metal aerogels and possible up-scaling. Lastly, preliminary ethanol oxidation tests demonstrated that morphology design extends to the catalytic performance. All in all, this work emphasizes the strengths of morphology design to obtain optimal structures, properties, and (performances) for any material application.

Introduction

Miniaturization and improved efficiency represent humanity's greatest aspirations, as evidenced in transistor technology,[1,2] automation,[3] or advanced materials[4] like catalysts.[5] The latter started with E. Davy, working on powdered platinum.[6] Realizing the benefits of a high surface area, research shifted toward various metal sheets, foams, gaze structures, and ultimately nanomaterials.[7] Aerogels, with their three-dimensional non-ordered structure of interconnected nanochains, are one final form of this process. They exhibit a ligament size (diameter of a nanochain) as small as a few nanometers/several atoms, hence scratching on the physical limit defined by the atom size. It further leads to melting point depression[8,9] and sparse mechanical stability,[10] the current drawbacks of metal aerogels.

In general, the aerogel state is a unique arrangement of matter, which is independent of the building material and synthesis procedure, except for individual elemental properties. Aerogels are characteristic for their high specific surface area (SSA) and broad pore size distribution, encompassing micro-, meso-, and macropores. This allows for efficient mass transport.[11] Compared to nanoparticles (NPs), metal aerogels are self-supporting, eliminating degradation and corrosion issues caused by the carrier material.[12,13] Moreover, they exhibit high selectivity, activity, and electric conductivity.[14–16] But most importantly, their modular structure preserves the nano-properties of the building blocks inside a macroscopic body.[11] All this makes metal aerogels excellent catalysts, particularly in electrocatalysis.

Based on the element distribution, multimetallic aerogels can be categorized similarly to NPs into three classes: hetero-structures, alloys (which include intermetallics as long-range-ordered alloys), and core–shell structures.[17–19] In the case of heterostructures, the elements separate spatially into different aggregates, which can alternate throughout the structure. Alloys consist of a mixture of elements, whereas intermetallics form

[a]*Physical Chemistry, TU Dresden, Zellescher Weg 19, Dresden 01069, Germany. E-mail: alexander.eychmueller@tu-dresden.de*

[b]*Institute of Ion Beam Physics and Materials Research, Helmholtz-Zentrum Dresden-Rossendorf e.V., Dresden 01328, Germany*

† Electronic supplementary information (ESI) available. See DOI: https://doi.org/10.1039/d3na00359k

strictly ordered compounds between at least two metals. Although core–shell structures technically fall under either class, they represent increased complexity, *e.g.*, classic core–shell particles or hollow spheres (HS). Depending on this classification, different element distributions result in unique features, including multiple reaction zones, tuning of properties between parent metals combined with synergistic effects, homogeneous structure, conservation of resources, and increased surface area.[20,21]

One- and two-step gelation by reducing metal salts in solution are the classical synthesis routes for metal aerogels. The former abstains from ligands, resulting in a transiently stable sol that spontaneously gels. That method allows fast reaction kinetics with minimal foreign ions. The two-step gelation, in turn, utilizes ligands to form a stable sol that only gels upon controlled ligand destabilization in a separate step. Although this method takes longer, it offers better control over each reaction step. Another versatile technique is galvanic replacement. In principle, it mimics a galvanic cell, that is, oxidation of the less noble metal NPs, while more noble metal ions undergo reduction. This creates small cavities in the NP surface, on which the more noble metal deposits as a protective layer. At this point, the reaction continues by dissolving metal within the cavities, forming a hollow core. Simultaneously, the NP outer layer constantly rearranges by alloying to minimize the lattice stress caused by continued metal deposition.[22]

Individual Au and Ni NPs have demonstrated a broad range of applications in various fields, including C–C coupling,[23] multiple oxidation[24–28] and reduction[29–31] reactions, or steam reforming.[32] When Au and Ni are combined, d-orbital coupling occurs, amplifying their element properties and enhancing the catalytic performance.[33–36] Moreover, and independent of the catalytic reaction, Au shows high catalytic activity at ambient temperature and mild conditions but is typically soft.[37] Introducing Ni in the system increases the integral stability.[38] This complementary effect is particularly important for aerogels, as it allows for gentle catalysis, preserving the porous structure and improving durability. Also to be mentioned is the high abundance and low cost of Ni.[39]

Besides miniaturization, metal aerogel performance is improvable by increasing its complexity. Various examples include aerogels made up of core–shell particles,[40–44] hollow spheres,[45–48] as well as hollow tubes,[49] nanoshells,[50] heterostructures,[51] or alloys.[52] Likewise, nanowires,[53–55] nanosheets,[56] dendrites,[57] and cuboids[58] were demonstrated as non-spherical building blocks. Doping,[59–62] lattice face control,[63,64] and 2D aerogels[65] offer even more potential for performance enhancement. However, most of these works predominantly focused on synthesizing and characterizing one particular morphology, either always using different element systems or disregarding comparisons with systems of the same elements. This is also well illustrated in a comprehensive comparison of bimetallic aerogels.[66] The consequence of these one-sided studies is the neglect of morphology as a central parameter, which remains unconnected to important parameters such as element composition and physicochemical properties. As a first step to address this problem, we used Au–Ni as a model system to synthesize different metal aerogel morphologies. This had multiple reasons: first, AuNi aerogels have not been previously reported, expanding the synthesis variety of metal aerogels. Second, an unknown system could be manipulated into different morphologies, emphasizing the potential of morphology design for any other element system. Common metal aerogel "morphologies" of alloys, heterostructures, and hollow spheres were obtained by using altered versions of the one-step gelation and the two-step gelation, with HS incorporating a galvanic exchange process into the two-step gelation. These transformed alloyed Au–Ni NPs, mixtures of pure Au and Ni NPs, and Au–Ni hollow sphere NPs into interconnected aerogel networks of nanowires, a combination of NPs and nanowires, and hollow spheres, respectively. In addition, the first two building blocks convert into nanochains and bigger NP aggregates. Since this morphological description is rather overloaded, hereafter, the categorization according to element distribution will be used to refer to the morphologies as well. Furthermore, certain synthesis parameters were optimized to obtain aerogels with the smallest possible yet homogeneous ligament size. Alloy aerogels focused on the metal and reductant concentration, while the heterostructure gels emphasized destabilization with electrolytes, and the HS gels again focused on the metal concentrations. This revealed some delicate structural trends for each morphology. Subsequently, the optimized morphologies were subjected to a comparative physicochemical characterization of crystallinity, element distribution, and porosity. These parameters were linked to the differences in morphology and their delicate structural trends, with most correlations drawn for nitrogen physisorption. Lastly, preliminary electrochemical tests regarding the ethanol oxidation reaction demonstrate that the linkage between morphology and structural properties directly extends to the catalytic performance.

Experimental

Chemicals

HAuCl$_4$·3H$_2$O (99.99%, Sigma-Aldrich), NiCl$_2$·6H$_2$O (99.9%, Sigma-Aldrich), NaBH$_4$ (granular, 99.99% Sigma-Aldrich), Na$_3$Cit (p.a., Merck), CaCl$_2$·2H$_2$O (p.a., Fluka), BaCl$_2$ (suprapur, E Merck AG), NaOH (p.a., Merck), Nafion (5 wt%, Sigma-Aldrich), EtOH (99%, 1% P, Berkel AHK), acetone (p.a., Sigma-Aldrich), and CO$_2$ (99.8%, Air Liquide) were used as received. MilliQ water (0.056 μS cm^{-1}) was provided by a coupled system of RiOs 8 and Milli-Q Academic from Millipore. Prior to use, 50 mM stock solutions for each metal salt were prepared in water.

Synthesis of Au$_3$Ni, AuNi, AuNi$_3$ alloy aerogels

Adopting the one-step gelation from Liu *et al.*[67] at first, the metal stock solutions (50 mM) were mixed in the molar proportions of Au$_3$Ni, AuNi, and AuNi$_3$. A 2 mL aliquot of these was diluted in 800, 400, 200, 100, and 50 mL H$_2$O and degassed for 30 minutes by N$_2$ perfusion. Simultaneously, a 50 mM NaBH$_4$ solution was prepared at a fixed ratio of reduction

equivalents to electron vacancies $n_{H^-} : n_{Me^{i+}}$ of 10, 12, and 14. The NaBH$_4$ solution was then swiftly added to the metal salt solution and stirred for 2 min at 450 rpm. The mixture immediately turned black. After two days, it formed a black gel at the bottom of the reaction vessel. The hydrogels are purified by solvent exchange with fresh H$_2$O seven times over two days. Finally, water was consecutively replaced with acetone, followed by an exchange to CO$_2$ (autoclave) to supercritically dry the solvogels at 37 °C and 90 bar. The underlined parameters represent standard conditions that were used if not stated otherwise (Fig. 1).

Synthesis of Au$_3$Ni, AuNi, AuNi$_3$ heterostructure aerogels

Taking inspiration from the two-step gelation method of Bigall et al.[16] we synthesized distinctive nanoparticles based on Herrmann et al.[68] (Au) and Wang et al.[69] (Ni). Briefly, in 40 mL water, concentrations of 3.75 mM citrate and 0.75 mM Ni^{2+} (diluted from stock solution) were set before degassing with N$_2$ for 60 min. Then, 2 mL of a degassed (N$_2$) aqueous NaBH$_4$ solution (150 mM) was added (2 mL min^{-1}; 450 rpm). A gradual change in color to yellow/brown indicated the formation of Ni NPs. In parallel, concentrations of 0.8 mM citrate and 0.75 mM Au^{3+} (diluted from stock solution) were set in 100 mL water before degassing and reduction by the addition of 1.16 mL fridge-cold mixed citrate (40 mM) and NaBH$_4$ (45 mM) solution. This resulted in a red Au NP sol. Subsequently, both NP solutions were mixed to reach a total metal concentration of 0.1 mmol in the following molar ratios: Au$_3$Ni, AuNi, and AuNi$_3$. The NP solutions were then gelled by the addition of 5 eq. NaBH$_4$ (or various other electrolytes, see ESI†) in relation to the total metal concentration, indicated by a slight brightening of the solution. After one day, a black gel formed, which was further processed the same as the alloy gels (Fig. 2).

Synthesis of AuNi$_3$, AuNi$_{4.4}$, AuNi$_6$ hollow sphere aerogels

The HS aerogels were fabricated using a modified version of the method described by Shang et al.[70] First, 50 mL of an aqueous solution containing 1.76, 1.92, 2.01 mM citrate and 1.007, 1.095, 1.150 mM Ni^{2+} ions were prepared according to the nominal compositions of AuNi$_3$, AuNi$_{4.4}$, and AuNi$_6$ respectively. After degassing with nitrogen for 60 min, 5 mL of an aqueous NaBH$_4$ solution (10.5 eq.) was added (2 ml min^{-1}; 450 rpm). The appearance of a brown/black color indicates the formation of NPs. After the complete addition of NaBH$_4$, the mixture was stirred for an additional 7 minutes before adding 2.5 mL of a 0.336, 0.247, and 0.192 mM Au^{3+} ion solution (1 mL min^{-1};
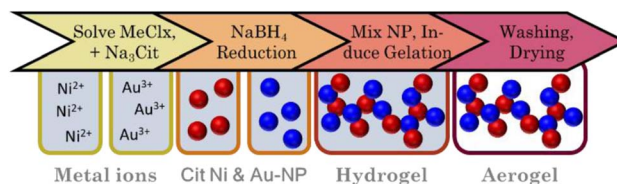

Fig. 2 Syntheses scheme of heterostructure Au$_x$Ni$_y$ aerogels.

450 rpm). The mixture was left to react for 3–4 days, during which the color changed from reddish brown to dark blue, indicating the completion of the galvanic replacement. Afterward, the HS NP solution was concentrated using polystyrene centrifuge filters (Sartorius, Vivaspin, 20 mL, MWCO 100000). Before use, the centrifuge filters were washed three times through centrifugation with water at 1000g (relative centrifugal force, 1 RCF = 1g). Then, the HS NP solution was stepwise concentrated by centrifugation at 300g for 15 min to reduce volume fractions of 20 mL to 5 mL. After complete concentration, the HS NP solution was washed three times by redispersion to 15 mL and centrifugation at 300g for 12 min. This step is crucial to remove impurities in the form of dissolved ions. In particular, Ni^{2+} ions can hinder further processing due to renewed reduction by NaBH$_4$, which is used as a destabilizing agent. After purification, the concentrated HS NP solution was redispersed to the original reaction volume, and 5 eq. NaBH$_4$ were added to induce gelation. A slight brightening of the solution indicated the beginning of gelation. After one day, a black gel formed, which was further processed equal to the alloy gels (Fig. 3).

Instruments and characterization

Supercritical CO$_2$-drying was performed in a model 13200J0AB autoclave from Spi supplies. For structural analysis, the gels were examined with a JEOL JEM-1400plus transmission electron microscope (TEM) equipped with an LaB$_6$ cathode and operated at an acceleration voltage of 120 kV. Likewise, an FESEM SU8020 scanning electron microscope (SEM) from Hitachi was used (2 kV, 10 μA). Energy-dispersive X-ray spectroscopy (EDX) was conducted using a silicon drift detector 80 X-MaxN from Oxford Instruments connected to the SEM (20 kV, 10 μA). The atomic compositions are determined as the mean of 16 measurements covering different parts of the sample. Crystallographic phase determination was carried out via a Bruker D2 Phaser powder X-ray diffractometer (Cu K 1.5406 Å). To measure the specific surface area, total pore volume (TPV), and pore size distribution of the aerogels, nitrogen physisorption
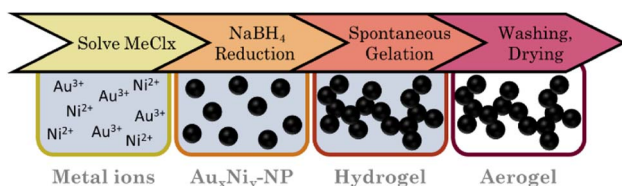

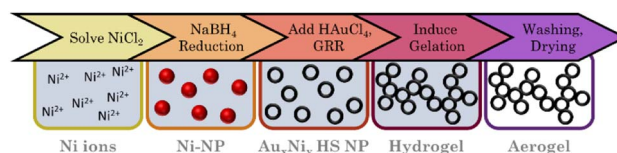Fig. 1 Syntheses scheme of alloy Au$_x$Ni$_y$ aerogels.

Fig. 3 Syntheses scheme of hollow sphere aerogels.

was performed at standard temperature (77 K) and pressure (1 atm) at $p/p_0 = 0.98$ on a model Nova 3000e from Quantachrome. The Brunauer Emmett Teller theory was applied to calculate the respective parameters, except for the pore size distribution, which was calculated using the Barrett Joyner Halenda theory. For nanoscale element composition analysis of the aerogels, high-angle annular dark-field (HAADF) scanning transmission electron microscopy (STEM) and spectrum imaging analysis based on EDX were conducted on a Talos F200X analytical electron microscope (FEI) operated at 200 kV and equipped with the ChemiSTEM technology for fast EDX acquisition, including four windowless silicon drift detectors (Super-X) and a high-brightness X-FEG electron source. Language improvements were made with Grammarly (free version) and DeepL by translating into German and back into English. Further, the AI chatbot ChatGPT was used to streamline the manuscript (prompt: please improve my text/writing, but keep it close to the original:…). Note that only short phrases or single words were adopted in the manuscript.

Electrode preparation and electrochemical characterization

The electrochemical measurements were conducted under an N_2 atmosphere at room temperature, using a three-electrode setup comprising a glassy carbon working electrode ($d = 3$ mm), an Ag/AgCl reference electrode (3.5 M KCl), and a Pt counter electrode. The system is controlled by a model PCSTAT128N potentiostat/galvanostat from Autolab. The electrodes are prepared from 3 μL of aerogel ink (mass concentration 7.54 mg ml^{-1}) by drop-casting and overlaying with 3 μL of a 0.5 wt% Nafion solution. For cyclic voltammetry (CV) measurements, a potential range from −0.4 to 0.6 V was scanned with a rate of 50 mV s^{-1} in a 2 M NaOH solution containing 0.25 M EtOH.

Results & discussion

Alloy aerogels by one-step gelation

Au–Ni alloy aerogels were successfully synthesized *via* one-step gelation. Note that the presence of alloys and heterostructures (next chapter) is confirmed only later (see Fig. 7). But to clearly distinguish the different morphologies, it is already used in this chapter. Regardless of their composition, a similar reaction behavior was observed in which the addition of the reductant triggers a rapid change in color from light yellow to reddish brown and ultimately black, accompanied by a strong H_2 gas evolution caused by hydrogen synproportionation.[71,72] This was followed by spontaneous gelation, resulting in a voluminous black precipitate within two days, similar to the findings of Bigall *et al.*[16] Likewise, TEM micrographs (Fig. 4) reveal similar structures of homogeneous, non-ordered, interconnected nanochain networks with vast interarticular pores and ligament sizes of 3–6 nm (ESI Fig. S1†).

By varying the element composition (Au$_3$Ni, AuNi, AuNi$_3$) and NaBH$_4$ excesses ($n_{H^-} : n_{Me^+} = 10, 12, 14$), two delicate structural trends/tendencies become apparent (Fig. 4A and ESI Fig. S1†). Firstly, the ligament size decreases with increasing Ni

content (≈ 2–3 nm), which correlates to the smaller lattice parameters of Ni (3.50 Å) compared to Au (4.07 Å).[73] Assuming that the intermediately formed NPs consist of a similar number of atoms for all three aerogels, this leads to smaller diameters for the Ni-rich NPs and, consequently, a decrease in aerogel ligament size with increasing Ni content. The second trend is a decrease in ligament size with increasing NaBH$_4$ excess (≈ 0–1 nm). A higher amount of NaBH$_4$ not only facilitates faster metal ion reduction but simultaneously increases the temporary ligand concentration, leading to the formation of smaller nanoparticles. Moreover, the prolonged stabilization time of the NPs shifts the system towards reaction-limited cluster aggregation (NPs do not necessarily fuse upon impact), which is governed by the hydrolysis of BH_4^-.[74] This shift leads to an increasingly incomplete gel network with higher NaBH$_4$ concentrations, resulting in disconnected nanochains and isolated NPs. In addition, aggregated spots were observed in the AuNi$_3$ sample. Based on the high contrast differences compared to the nanochain fragments, the NPs appear to be enriched with Au. This segregation may be due to a combination of the shift to reaction-limited cluster aggregation and the miscibility gap between Au and Ni, which makes Au more susceptible to coalescence.[75] One might think these ligament size trends are unique to Au–Ni aerogels. However, we have also observed them in Au–Cu aerogels (ESI Fig. S2†). For the same reasons, namely a smaller lattice parameter of Cu (3.60 Å)[73] compared to Au and the shift towards reaction-limited cluster aggregation, the ligament size decreases with increasing Cu content and NaBH$_4$ concentration. Au–Ni and Au–Cu differ only in the appearance of discontinued gel strands and copper oxide needles. This relates to the phase diagram of Au–Cu consisting of discrete phases instead of a wide miscibility gap as for Au–Ni.[76] Hence, suggesting element-specific changes in the gelation mechanism, however, seemingly not affecting the ligament size trends. In order to retain the advantages of a high NaBH$_4$ excess (12 eq.), the total metal concentration was adjusted to promote complete gelation. This was first tested for the Au$_3$Ni gel with total metal concentrations of 0.05 mmol, 0.2 mmol, and 0.4 mmol (Fig. 4B and ESI Fig. S3†). As hypothesized, higher total metal concentrations resulted in increasingly incomplete gelation. At 0.4 mmol and above, network defects were no longer observed. In a higher concentrated reaction media, the mean free path between the individual NPs is reduced, leading to an increased number of collisions and a higher probability of NPs fusing together. The same applies to nucleation. Furthermore, the gelation time was reduced to as low as 12 h while preserving the small ligament size. Besides, the higher collision rate causes a transition of particulate to smooth gel strands. While in dilute reaction media, the NPs have a higher chance of sticking together loosely, reducing their fusion area.

Since a total metal concentration of 0.4 mmol provided complete gelation for Au$_3$Ni, it was also applied to AuNi and AuNi$_3$ (ESI Fig. S4†). Likewise, they fully gel, retain their ligament size and show no aggregated spots. Beyond that, they exhibit the same trend as discussed in Fig. 4A. In addition to the structural improvements, up-scaling by increasing the metal concentration offers significant technical advantages. For
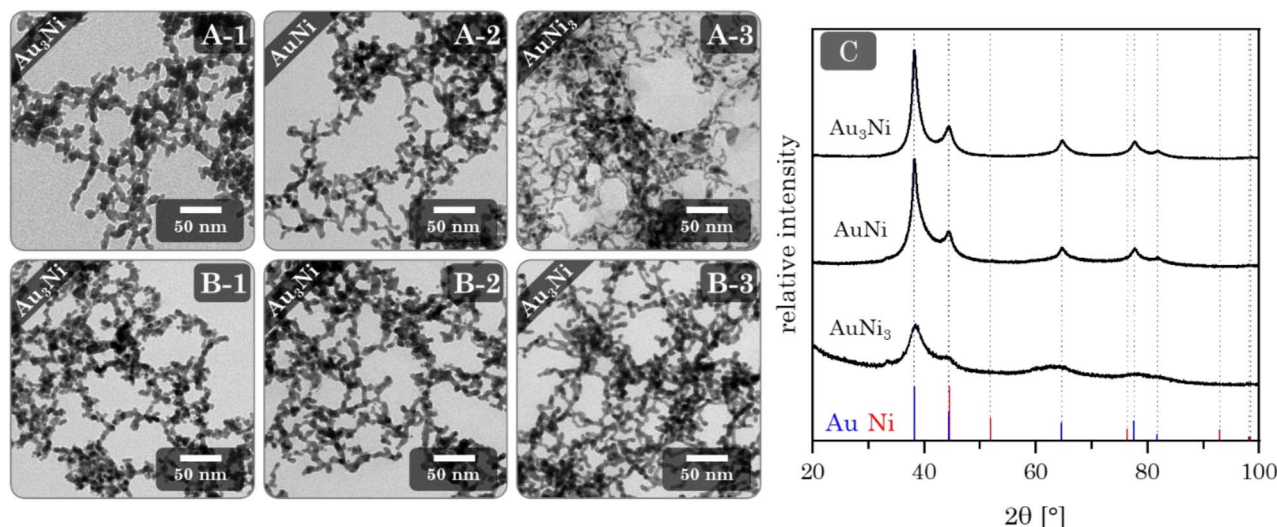
Fig. 4 TEM micrographs of Au$_3$Ni, AuNi, and AuNi$_3$ aerogels reduced with 10 eq. (A-1), 12 eq. (A-2), and 14 eq. (A-3) NaBH$_4$, respectively, as well as Au$_3$Ni gels synthesized at constant NaBH$_4$ excess (12 eq.) and total metal concentrations of 0.05 mmol (B-1), 0.2 mmol (B-2), and 0.4 mmol (B-3). All gels exhibit a fine and homogeneous network structure, where increasing the concentration of the NaBH$_4$ excess and Ni content leads to smaller ligament sizes. A higher concentrated reaction media, on the other hand, facilitates complete gelation. The XRD patterns show one crystalline phase with Bragg reflections close to those of Au (C).

instance, the solvent volume was reduced to a quarter, simultaneously saving resources and producing less waste. Moreover, this procedure facilitates faster production rates compared to the standard synthesis.[68] Depending on the required ligament size, even further concentration is possible.

Alternatively, ethanol can be used as a reaction medium with faster gelation kinetics. The lower dielectric constant (16.2) compared to H$_2$O (80.3) leads to the formation of smaller solvent shells, resulting in faster gelation.[77–79] Although this approach facilitates complete gelation to similar networks as described before, the ligament size and corresponding size distribution are significantly larger ($\approx$6–11 nm) (ESI Fig. S5†).

The final compositions of the aerogels were validated by EDX measurements (ESI Table S1†). While nominal and final compositions are generally close, minor deviations of up to 4 at% occur. This may be caused by slight oxidation and subsequent detachment of Ni from the network during the aerogel synthesis.

Phase analysis by XRD (Fig. 4C) reveals a single crystalline phase with Bragg peak positions between those of Au and Ni. Notably, and independent of their composition, they only show a minuscule shift to higher angles compared to the Au reference position. This observation is in accordance with the wide miscibility gap between Au and Ni, which only allows stable phases of the nearly pure elements (spinodal decomposition). Therefore, Ni can be incorporated more easily into the Au lattice than *vice versa*.[38,75] This stable Au-rich crystalline phase is expressed by the small angular shift. The absence of the Ni-rich phase could be due to oxidation and subsequent dissolution, which relates to the slight loss of Ni in the final composition and a strong oxidation behavior (see next chapter). The remaining Ni of a random Au:Ni composition may form an amorphous phase within the miscibility gap, resulting in an X-ray amorphous behavior.

Heterostructure aerogels by two-step gelation

The first step to synthesizing the heterostructure aerogels *via* two-step gelation was preparing the corresponding NPs. For Au, stable NPs (red solution) with an average size of (3.3 $\pm$ 0.8) nm (Fig. 5A-1) form, while the Ni NPs (brown solution) have a slightly larger diameter of (7.0 $\pm$ 1.6) nm. However, Ni NPs (citrate-capped) tend to aggregate (Fig. 5A-2) and completely dissolve in O$_2$-containing aqueous solutions in just a few hours (ESI Fig. S6†). Tests on this dissolution behavior showed that the stability of Ni NPs was only 1 h before a significant loss occurred, indicated by a decolorization of the solution. Consequently, the following experiments were performed by rapid destabilization under the exclusion of air. Whether or not destabilization is successful depends strongly on the electrolyte species.[43,80,81] To gain an overview, firstly, Ni NPs were destabilized with various electrolytes. Those potent enough to facilitate gelation were subsequently applied to Au NPs and the mixture of both (ESI Fig. S7†). Promising results were obtained with chloride-containing bivalent electrolytes such as CaCl$_2$, BaCl$_2$, and MgCl$_2$. However, EDX measurements revealed the absence or a significant loss of Ni in the final structure (ESI Table S2†). Thus, either during or after gelation, the Ni NPs still dissolve, leaving behind a pure Au gel. Although the electrolytes could not be used for further destabilization, they contributed to expanding the Hofmeister series on metal aerogels.[43]

In contrast, NaBH$_4$ is a special electrolyte that not only facilitates gelation but simultaneously keeps Ni inside the nanoparticle assembly. NaBH$_4$ increases the ionic strength but also has reducing properties, resulting in a certain depot effect. If Ni NPs are oxidized during or after the synthesis, they will be immediately reduced again as long as the reducing agent is present. In addition, the reaction vessels are sealed, causing the
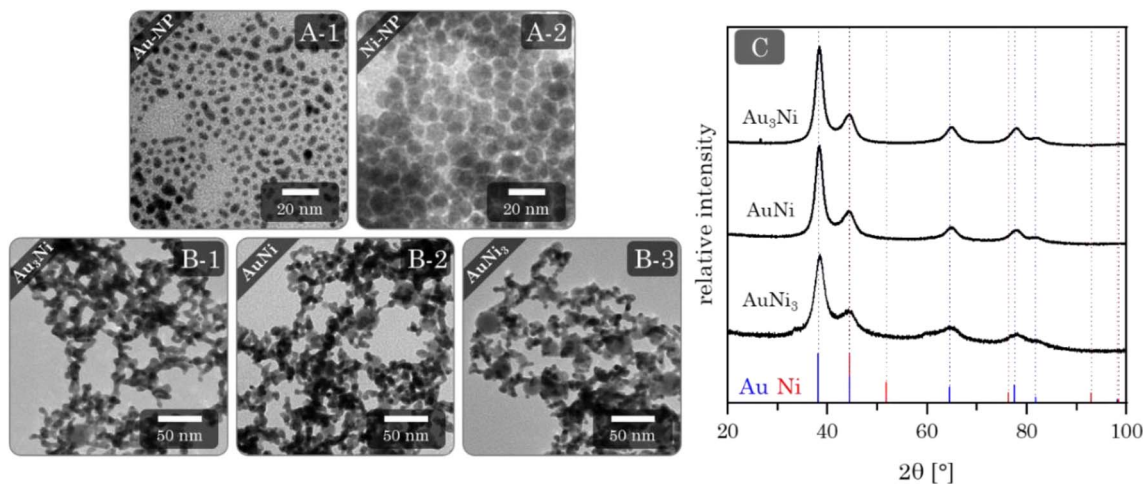
Fig. 5 TEM micrographs of the primary Au NPs (A-1) and Ni NPs(A-2). Furthermore, TEM micrographs of the Au$_3$Ni (B-1), AuNi (B-2), and AuNi$_3$ (B-3) gels destabilized by 5 eq. NaBH$_4$ show a bipartite structure of seamlessly connected nanochains and NPs. The latter increased in number as the Ni content increased. This indicates that the nanowires contain more Au, as more Ni is integrated into the nanoparticles. The XRD patterns show only one crystalline phase with Bragg reflections close to those of Au (C).

build-up of H$_2$ gas and a slight overpressure, protecting the reaction medium from O$_2$ entry.

Upon addition of NaBH$_4$ to the reddish brown Au and Ni NP mixture, the solution initially brightens before slowly turning grey. After two days, voluminous monolithic black precipitates form, showing a distinct bipartite structure in TEM micrographs (Fig. 5B). It consists of randomly interconnected NPs and nanochains that form an overarching gel network. As expected, there are no size-dependent structural trends due to the same building blocks of all compositions. This results in ligament sizes of approx. 5 nm for nanochains and diameters between 15 and 30 nm for NPs. Notably, the number of NPs increases with increasing Ni content, indicating that Ni makes up the bulk of the NPs. Surprisingly, this is not expected from the literature, which suggests that mixed pure NPs would form hybrid gel strands during gelation.[51] Such a unique network was observed for the first time and may be attributed to the miscibility gap that prevents the formation of mixed gel strands.

Similar to the alloy gels, small deviations of 6–10 at% between the nominal and final element composition were found by EDX measurements (ESI Table S1†). Again, this is due to the oxidation and subsequent dissolution of Ni from the gel structure. However, the deviation is more pronounced in this case because of the intrinsic separation of Au and Ni in individual NPs, facilitating oxidation/dissolution of Ni.

The XRD patterns (Fig. 5C) show similar results compared to the alloy gels. All Bragg reflections point to a single phase whose positions lie between the Au and Ni reference, with only minimal shifts to higher diffraction angles. This can be expected due to a comparable influence of the miscibility gap, with the assumption of separation of Au and Ni further supporting this effect. Surprisingly, no Ni or possible nickel oxides are observed as secondary crystalline phases. That leads back to the assumption that X-ray amorphous proportions are present in the aerogels.

Hollow sphere aerogels by two-step gelation coupled with galvanic replacement

Adding Au^{3+} ions to a freshly synthesized Ni NP solution resulted in an immediate color change from brown to black. After the complete addition of Au^{3+} ions, the solution is dark brown and gradually changes to an intensive blue over the next four days. TEM micrographs (Fig. 6A) reveal exclusive HS NPs with a size of (33.6 ± 9.5) nm, (29.3 ± 7.7) nm, and (27.6 ± 3.4) nm, respectively, for the AuNi$_3$, AuNi$_{4.4}$, and AuNi$_6$ HS NPs. All show a broad hollow interior. The galvanic replacement occurred uniformly in each NP as well as in the overall system. These observations are consistent with the mechanism described above.[22] The nominal metal composition and ratio of Au^{3+} ions to Ni NPs exert a significant influence on the structural properties of the resulting HS NPs. As the Ni content increases, the shell thickness and particle diameter decrease, and the particle size distribution narrows. This correlates with the number of Ni NPs in relation to the Au^{3+} ions. When the Au^{3+} ions are less abundant, fewer react per NP, gradually thinning the shell and the overall NP size. However, the decrease in HS NP size is too large to be attributed to the nominal composition alone. An additional effect must be assumed. One possible explanation is light compression during the alloying process, which is less pronounced in NPs with thicker shells due to higher internal stability. The trend in size distribution can be attributed to the surface roughness of the NPs, which is amplified depending on the shell thickness.

If the degassing time of the initial Ni NPs is prolonged, from 7 to 60 min, more fractured and particulate hollow spheres are formed (ESI Fig. S8†). This is likely due to the onset of oxidation, which blocks some facets for Au deposition and causes a flake-like shell. Since the resulting HS NPs are rather large, smaller Ni NPs were synthesized and processed with galvanic replacement (ESI Fig. S9†).[48,69] Although this yielded a minority of HS NPs, they occurred in a mixture with solid NPs, core–shell NPs, ring
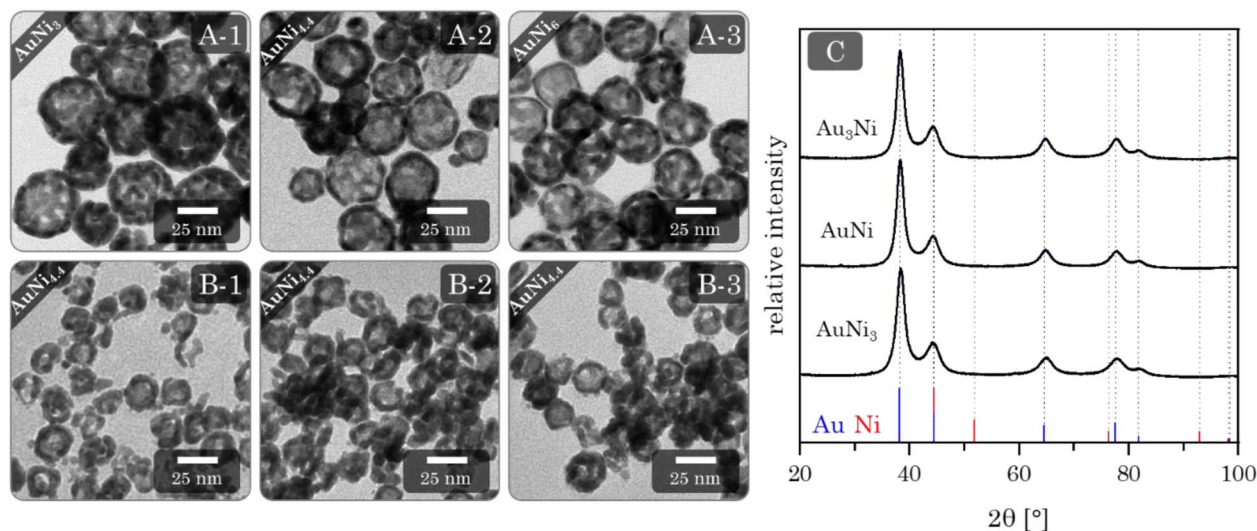
Fig. 6 $AuNi_3$ (A-1), $AuNi_{4.4}$ (A-2), and $AuNi_6$ (A-3) HS NPs before and $AuNi_{4.4}$ HS NPs after gelation with 0 eq. (B-1), 2.5 eq. (B-2), and 5 eq. (B-3) $NaBH_4$. Before gelation, the HS NPs show a homogeneously formed shell with an empty core. An increase in the nominal Ni content causes a narrowing of the HS NP size, shell thickness, and size distribution. After gelation, significant compression of the HS NPs has taken place. The XRD patterns reveal only one crystalline phase with Bragg reflections close to those of Au, as predicted by the composition (C).

structures, or big agglomerates. This limited success could be due to the additional shrinking effect described above, which may be more pronounced for smaller NPs. In addition, oxidation occurs faster and more intensively for smaller Ni NPs. This indicates a strong dependence of the galvanic replacement on the initial (sacrificial) size of the NPs. Another crucial step in the synthesis is centrifugation, which serves as a pretreatment for destabilization/gelation. This induces considerable mechanical stress on the NPs. Even at mild conditions of 300 g, the $AuNi_{4.4}$ HS NPs contract to diameters of approx. 16 nm. This effect can be attributed solely to centrifugation, as the contraction occurs independently of the addition of electrolytes. Although the hollow spheres gel by redispersion alone, adding a small amount of electrolyte can increase the contact area between the HS building blocks. Hence, adding electrolytes is a gentle method to improve the connectivity without putting further stress on the HS NPs during gelation. This results in homogeneous, non-ordered networks of interconnected hollow spheres (Fig. 6B). As an alternative to $NaBH_4$: $CaCl_2$ and $BaCl_2$, which had been identified as potent destabilizing agents for heterostructure gels, were successfully used to promote the destabilization of HS NPs with subsequent gelation (ESI Fig. S10†).

In contrast to the other morphologies, the HS aerogels display a strong deviation between the nominal and final element compositions, ranging from 50 to 65 at%. Moreover, the final ratios are very close to each other, falling in between $Au_{80}Ni_{20}$ and $Au_{90}Ni_{10}$ (ESI Table S1†). This can only be explained by the pronounced oxidation and dissolution of Ni from the gel network. Considering the color change from dark brown to blue, it is most likely that specifically non-alloyed Ni dissolves during this period. For clarity, the nominal metal ratios will continue to be used for naming the aerogel samples.

XRD phase analysis (Fig. 6C) shows the same characteristics as the alloy and heterostructure gels. All Bragg reflections

correspond to a single phase inbetween the positions of the Au and Ni reference Bragg peaks. Again, with a slight shift to larger angles compared to Au. This is in line with the EDX results, as only a small amount of Ni remains in the final gel. However, the effect of the miscibility gap may also be relevant.

Further physiochemical characterization

Regardless of the synthesis procedure and the resulting morphology of the Au–Ni samples, SEM micrographs (Fig. 7I and ESI Fig. 11–13A, B) reveal a typical three-dimensional sponge-like aerogel structure and further confirm the morphologies observed in previous TEM micrographs. Fig. 7 provides an overview of the different morphologies. Different aerogel compositions of the same morphology are compared in the ESI Fig. S11–S13.† The alloy gels exhibit homogeneous interconnected nanochains, whereas the heterostructure gels display a bipartite network comprising nanochains and nanoparticles. Significant contrast differences in backscattered electron imaging confirm the separation of both elements into Ni-rich NPs and Au-rich nanochains, whereby the number of NPs increases with increasing Ni content. In the case of HS gels, interconnected HS building blocks are observed, while high-magnification SEM micrographs display the hollow-spherical character. Moreover, the element distribution on the nanoscale was monitored by spectrum imaging analysis based on EDX in scanning TEM mode (Fig. 7(2) and ESI Fig. S11–13C†). In the alloy gels, both elements are fairly homogeneously distributed throughout the whole gel network and individual gel strands. However, there may be a slight tendency for Ni to be located closer to the surface. This observation resonates with the slight loss of Ni in the final compositions and would support the formation of an oxide layer. In the heterostructure gels, the nanochains consist predominantly of Au but are evenly doped
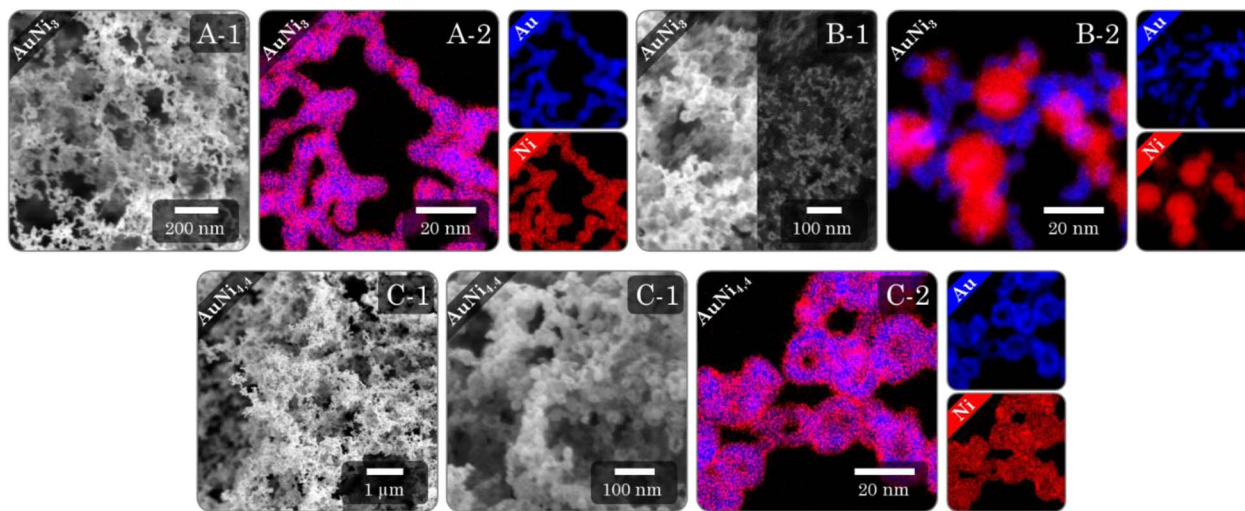
Fig. 7 SEM micrographs (1) and STEM-EDX-based element mapping (2) of the alloy AuNi$_3$ (A), heterostructure AuNi$_3$ (B), and HS AuNi$_6$ (C) aerogels. All samples exhibit a sponge-like gel character regardless of their morphology. Moreover, the structural trends observed by TEM reappear. Alloy gels and HS gels show fairly homogeneous element distributions (with enhanced Ni signals at the surfaces), while in the heterostructure gels, the elements separate into Ni NPs and Ni-doped Au nanochains.

with small amounts of Ni. Although the gels can not be considered a heterostructure of Au nanochains and Ni NPs anymore, they can still be considered a heterostructure of Ni NPs and Ni-doped Au nanochains, with a clear interface between NPs and nanochains. The doping with Ni is likely due to the use of NaBH$_4$ as a destabilizing agent, which also reduces leftover Ni^{2+} ions. The NPs, on the other hand, consist entirely of Ni. Again, it becomes clear that the NPs are entangled by several nanochains forming a bipartite morphology. The structure is also covered with an oxide layer, which has a larger thickness compared to the alloy aerogels (especially for the Ni NPs), explaining the higher deviation in the final composition. The HS gels, which essentially are alloy gels with a special hierarchical morphology, exhibit the same behavior. A homogeneous distribution of Au and Ni is observed, while Ni is slightly more abundant at the inner and outer surfaces of the hollow spheres. Likewise, they are covered with an oxide layer.

The physical characterization for each Au–Ni morphology and composition is completed by nitrogen physisorption (Fig. 8A and ESI Fig. S14A†). All isotherms exhibit characteristics of type II/IV behavior arising from the simultaneous presence of micro-, meso-, and macropores.[82] These pores are formed as interparticle spaces between nanochains, NPs, hollow interiors, or a combination thereof. Although multi-layer adsorption becomes progressively less favorable as p/p_0 decreases, most isotherms do not adhere to the BET theory since their hysteresis fails to close at $p/p_0 = 0.42$. One possibility is a breathing effect of the entire aerogel, whose network swells upon adsorption and shrinks upon desorption. That is supported by measurements and calculations from Reichenberger *et al.* taken for silica aerogels.[83,84] Another factor contributing to hysteresis is the possibility of N$_2$ retention by pore blockage or bottleneck pores. This is less relevant for loose networks such as the alloy and heterostructure gels, but the interior voids of the HS gels can act as such bottleneck pores, as evidenced by their broader hysteresis loop.

Consequently, the pore type and morphology are directly related to hysteresis. As a result, hysteresis closes first for more spacious networks, with the order being: heterostructure, alloy, and HS gels. It should be noted that increasing the Ni content causes the hysteresis to close at a higher p/p_0.

The pore size distribution (Fig. 8B and ESI Fig. S14B†) of all morphologies shows the expected broad spectrum of meso- and macropores, while micropores are recorded as surface roughness, including smaller mesopores (up-down pattern). This minimizes diffusion barriers and allows for efficient mass transport. Equally important, the size distribution of mesopores can serve as a fingerprint of a particular morphology. Alloy gels consist largely of small mesopores formed in the interparticle spaces between nanochains. In Heterostructure gels, the interparticle spaces are more complex due to the mixture of nanochains and NPs, resulting in high proportions of smaller and larger mesopores. Lastly, HS gels, which again are based on only one building block, form predominantly small mesopores, but their hollow interiors provide additional medium-sized mesopores.

The aerogels show a wide range of SSAs between 30 and 100 m^2 g^{-1} (Fig. 8C-1), increasing from HS gels to alloy gels to heterostructure gels. This order is due to the slightly larger shell thickness of the HS gels (3–6 nm) compared to the ligament size of the alloy gels (3–4 nm). Although the same is true for heterostructure gels, their bipartite structure allows for nearly free-standing NPs and shortened nanochains that expose more surface area. Moreover, there is a general trend across all morphologies whereby the specific surface area increases with increasing Ni content. This connects back to the structural discussion of individual morphologies. For the alloy and HS gels, the ligament size or building block diameter and shell thickness decrease, while the heterostructure gels transition to a higher number of NPs and nanochains, which are also shortened in length. However, this effect cannot explain the exceptionally high SSA of the AuNi$_3$ alloy gel. One possibility is
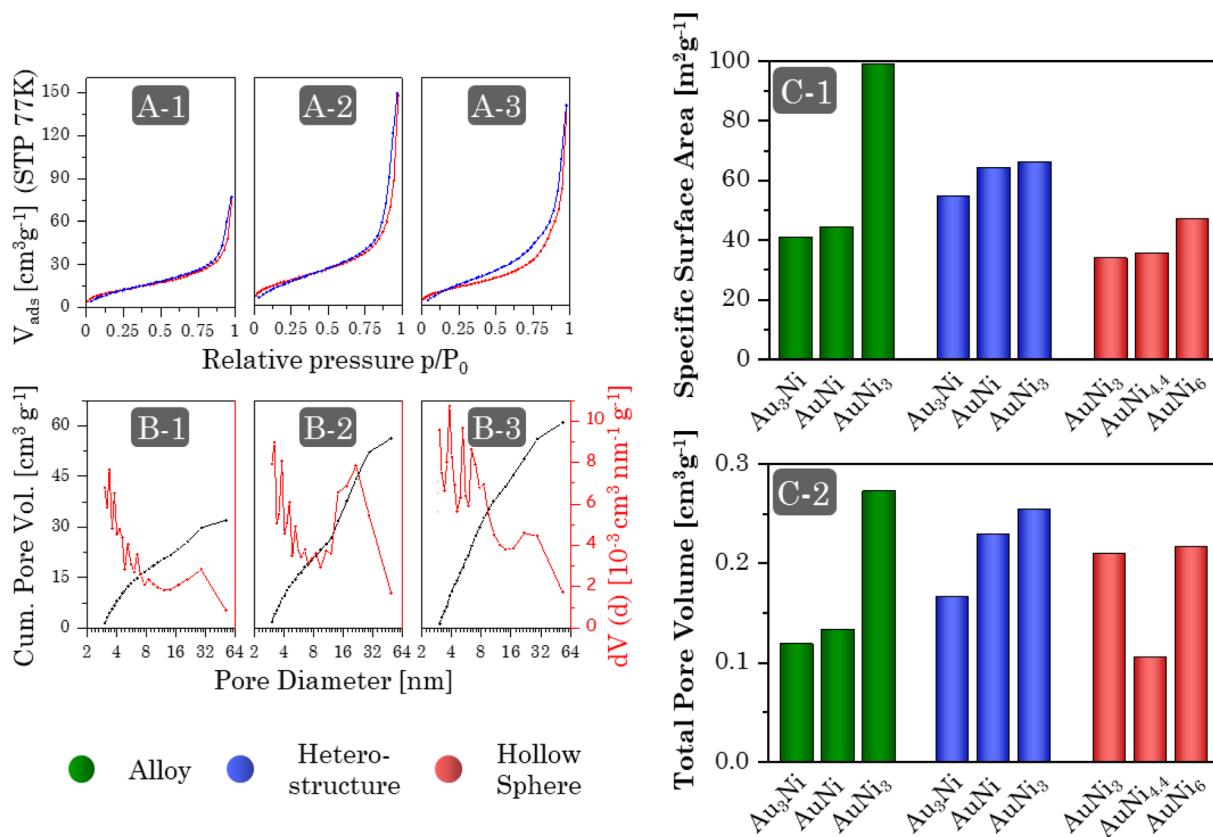
Fig. 8 Representative N_2 physisorption isotherms (A) and pore size distributions (B) of the alloy AuNi (1), heterostructure AuNi (2), and HS $AuNi_3$ (3) aerogels measured at STP (standard temperature at 77 K and pressure). All isotherms show a characteristic mixture of type II/IV behavior caused by a broad distribution of micro-, meso-, and macropores. In addition, the pore size distribution and isotherm shape are greatly influenced by the morphology. The SSA (C-1) and TPV (C-2) mostly show the same dependency on the morphology, which usually increases with increasing Ni content due to shrinking building blocks or their increase in number or size.

the formation of a porous oxide layer, which is supported by the slightly higher Ni concentration at the surface. It is noteworthy that prolonged storage of the gel in the air leads to the development of a white shimmer.

The total pore volume (Fig. 8C-2) of most aerogels also increases with increasing Ni content, following the same structural dependence as the SSA. As already indicated by the pore size distribution, the alloy gels exhibit the lowest TPV of approx. 0.125 cm^3 g^{-1} due to the absence of larger mesopores. On the other hand, heterostructure and HS gels have a higher TPV of approx. 0.2 cm^3 g^{-1}. In particular, the heterostructures exhibit a strong dependence on the element ratio, which correlates with the number of NPs and nanochains. Similar to the SSA, the TPV of the Au_3Ni gel also proves to be larger than expected. Likewise, the $AuNi_{4.4}$ HS gel does not follow the TPV trend. Part of the reason may be a temperature effect, as the samples were synthesized during different seasons, potentially intensifying the stress during centrifugation for $AuNi_{4.4}$.

Preliminary ethanol oxidation reaction catalysis

With the successful synthesis of Au–Ni aerogels in three different morphologies and elemental compositions, the influence of both factors on the electrochemical properties was

investigated in initial tests, using ethanol oxidation as an example. Stability tests revealed (Fig. 9) that each morphology exhibits a unique CV shape that depends on the element composition. This, in turn, affects current density and stability. Alloy and HS gels have already shown similarities in their structural trends, and the same is true for their catalytic behavior. Both show two redox pairs at around 0.17/0 V and 0.38/0.22 V for the alloy gels and 0.1/0.05 V and 0.45/0.38 V for the HS gels. The former are respectively assigned to the Ni/Ni^{2+} redox pair and the latter to Ni^{2+}/Ni^{3+}. Ethanol oxidation occurs shortly after oxidation to Ni^{3+}, also indicated by the absence of a corresponding reduction peak. In contrast, the heterostructure gels show only a mixed redox pair around 0.5/0.28 V, accounting for both Ni^{2+}/Ni^{3+} and ethanol oxidation. This is caused by an increased abundance of NiO, which can directly be converted to NiOOH. Ni, in turn, is first converted into the intermediate $Ni(OH)_2$ and only then to NiOOH. This is consistent with Ni/NiO nanoparticles on carbon supports.[85] Thereby, NiOOH possibly enhances the catalytic reaction by mediating protons and electrons.[86] However, its potential could not be fully utilized in the heterostructure gels because the NiO regions are spatially separated from Au, preventing their synergistic effects.
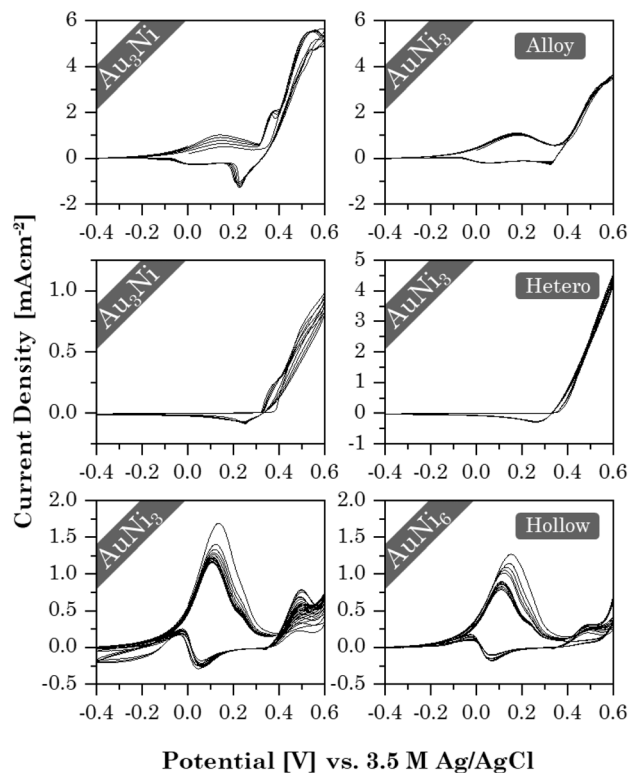
Fig. 9 Cyclic voltammetry of the Au_3Ni, $AuNi_3$ alloy, and hetero-structure gels as well as the $AuNi_{4.4}$ and $AuNi_6$ HS gels. Depending on the morphology, the gels display a specific CV shape. Both the alloy and HS gels show two redox pairs of Ni/Ni^{2+} and Ni^{2+}/Ni^{3+} and ethanol oxidation shortly after the second. However, the HS gels exhibit lower stability caused by the depletion of Ni. The heterostructure gels, on the other hand, only show one mixed peak of Ni^{2+}/Ni^{3+} and ethanol oxidation close to Ni/NiO on carbon.

The current density decreases from the alloy (6 mA cm^{-2}) to the HS (2 mA cm^{-2}) to the heterostructure gels (1 mA cm^{-2}). This indicates a dependence on the element (composition and) distribution. Although the alloy and HS gels have a fairly homogeneous element distribution, the latter contains a higher Au content combined with a lower SSA. Consequently, less NiOOH is formed to support catalysis. This is not the case for the heterostructures, but the spatial separation of the elements throttles the synergistic effects.

The highest cycling stability is observed for the heterostructure gels, owing to their segregated structure that allows for a smooth reintegration of temporarily oxidized Ni in the aerogel network. While the random element distribution allows the same in alloy gels, a significant decrease is observed for the HS gels. When nickel oxidizes, the HS structure may rearrange to minimize lattice stress. As a result, Ni is less likely to be reintegrated into the HS than to be accumulated on the surface or deposited in the electrolyte.

Although increasing the Ni content does not affect the heterostructure gels, the current density of the alloy and HS gels decreases slightly. It is likely that the more Ni is present in the gel, the more the CV shape slowly shifts toward the heterostructure behavior as thicker oxide layers form, increasingly separating the elements. While this provides some initial

insight into the effect of morphology and element distribution on catalysis, more in-depth studies will be needed.

Compared with the literature, the Au–Ni gels show a rather poor performance.[87,88] But this can be neglected in this study as the important part to illustrate the impact of morphology design on the catalytic performance was clearly demonstrated.

Conclusions

Au–Ni aerogels were successfully developed as a new element system of metal aerogels. Moreover, the synthesis was effectively manipulated to yield three common metal aerogel morphologies: alloys, heterostructures, and hollow spheres. Of particular note, our heterostructures are unique in that they consist of a coherent network of NPs and nanochains, distinguishing them from previously reported morphologies that only contain nanochains. In addition, several subtle structural trends related to the Au–Ni aerogels of each morphology were identified. They all allow tailoring of the respective structural parameters. These differences in morphology, in conjunction with the subtle structural trends, were revealed to directly affect the physico-chemical and catalytic properties. This can be particularly beneficial in gaining new insight into known materials or developing new ones. This is underlined by some trends seemingly not depending on the element system, such as the ligament size, so they may apply to metal aerogels in general.

N_2-physisorption and STEM-EDX further highlighted differences among the individual aerogel morphologies, which were evident in different element distributions and porosities. Accordingly, the morphological differences and trends observed by electron microscopy were directly related to changes in physisorption behavior. The isotherm and pore size distribution serves as a fingerprint for each morphology. A similar relationship between the morphology and catalytic behavior of the aerogels is evident in preliminary ethanol oxidation reaction experiments, as reflected by changes in current density and cycling stability.

This study proves that morphology design is a versatile tool to introduce and control certain physicochemical characteristics, which in turn affect the catalytic performance. This is complementary to a thoughtful fine-tuning of the synthesis parameters. However, morphology was considered rather linguistically and linked to specific structural features and trends observed in TEM micrographs. In future works, it would be desirable to establish a quantitative measure for the morphology of metal aerogels, similar to the K-index developed by Leventis et al. for polyurethane gels.[89] Such measure would act as a predictor, descriptor, and correlator between morphology and physicochemical properties.

Conflicts of interest

There are no conflicts to declare.

Acknowledgements

Notes and references

1 W. F. Brinkman, D. E. Haggan and W. W. Troutman, *IEEE J. Solid-State Circuits*, 1997, **32**, 1858–1864.

2 F. Wu, H. Tian, Y. Shen, Z. Hou, J. Ren, G. Gou, Y. Sun, Y. Yang and T.-L. Ren, *Nature*, 2022, **603**, 259–264.

3 C. P. Janssen, S. F. Donker, D. P. Brumby and A. L. Kun, *Int. J. Hum. Comput. Stud.*, 2019, **131**, 99–107.

4 B. Giese, M. Drapalik, L. Zajicek, D. Jepsen, A. Reihlen and T. Zimmermann, *Advanced Materials: Overview of the Field and Screening Criteria for Relevance Assessment*, Wien, Hamburg, 2020.

5 J. M. Domínguez-Esquivel and M. Ramos, *Advanced Catalytic Materials: Current Status and Future Progress*, Springer Nature Switzerland AG, Cham, 2019.

6 E. Davy, *Philos. Trans. R. Soc. London*, 1820, **110**, 108–125.

7 W. Y. Teoh, A. Urakawa, Y. H. NG and P. Sit, *Heterogeneous Catalysts: Advanced Design, Characterization and Applications*, Wiley-VCH, Weinheim, 2021.

8 M. Liu and R. Y. Wang, *Sci. Rep.*, 2015, **5**, 16353–16361.

9 T. Castro, R. Reifenberger, E. Choi and R. P. Andres, *Phys. Rev. B: Condens. Matter Mater. Phys.*, 1990, **42**, 8548–8556.

10 K. Schneider, I. Melnyk, K. Hiekel, A. Fery, G. K. Auernhammer and A. Eychmüller, *J. Phys. Chem. C*, 2019, **123**, 27651–27658.

11 C. Ziegler, A. Wolf, W. Liu, A. K. Herrmann, N. Gaponik and A. Eychmüller, *Angew. Chem., Int. Ed.*, 2017, **56**, 13200–13221.

12 S. Henning, H. Ishikawa, K. Laura, J. Herranz, M. Elisabeth, A. Eychmüller and T. J. Schmidt, *Angew. Chem., Int. Ed.*, 2017, **56**, 10707–10710.

13 H. Schulenburg, B. Schwanitz, N. Linse, G. G. Scherer, A. Wokaun, J. Krbanjevic, R. Grothausmann and I. Manke, *J. Phys. Chem. C*, 2011, **115**, 14236–14243.

14 I. Zuburtikudis and H. Saltsburg, *Science*, 1992, **258**, 1337–1339.

15 *Nanoparticles and Catalysis*, ed. D. Astruc, WILEY-VCH Verlag GmbH & Co. KGaA, 2008.

16 N. C. Bigall, A.-K. Herrmann, M. Vogel, M. Rose, P. Simon, W. Carrillo-Cabrera, D. Dorfs, S. Kaskel, N. Gaponik and A. Eychmüller, *Angew. Chem., Int. Ed.*, 2009, **48**, 9731–9734.

17 D. Wang and Y. Li, *Adv. Mater.*, 2011, **23**, 1044–1060.

18 S. E. Skrabalak, J. Chen, S. Neretina and D. Qin, *Part. Part. Syst. Charact.*, 2018, **35**, 1800111–1800113.

19 T. Dang-Bao, D. Pla, I. Favier and M. Gómez, *Catalysts*, 2017, **7**, 207–240.

20 G. Li, W. Zhang, N. Luo, Z. Xue, Q. Hu, W. Zeng and J. Xu, *Nanomaterials*, 2021, **11**, 1926–1963.

21 A. M. El-Toni, M. A. Habila, J. P. Labis, Z. A. ALOthman, M. Alhoshan, A. A. Elzatahry and F. Zhang, *Nanoscale*, 2016, **8**, 2510–2531.

22 X. Xia, Y. Wang, A. Ruditskiy and Y. Xia, *Adv. Mater.*, 2013, **25**, 6313–6333.

23 G. Li and R. Jin, *Nanotechnol. Rev.*, 2013, **2**, 529–545.

24 A. J. Motheo, S. A. S. Machado, F. J. B. Rabelo and J. R. Santos Jr, *J. Braz. Chem. Soc.*, 1994, **5**, 161–165.

25 A. F. B. Barbosa, V. L. Oliveira, J. Van Drunen and G. Tremiliosi-Filho, *J. Electroanal. Chem.*, 2015, **746**, 31–38.

26 P. Rodriguez, D. Plana, D. J. Fermin and M. T. M. Koper, *J. Catal.*, 2014, **311**, 182–189.

27 S. A. C. Carabineiro, *Front. Chem.*, 2019, **7**, 1–32.

28 M. Simões, S. Baranton and C. Coutanceau, *J. Phys. Chem. C*, 2009, **113**, 13369–13376.

29 M.-J. Sun, Z.-W. Gong, J.-D. Yi, T. Zhang, X. Chen and R. Cao, *Chem. Commun.*, 2020, **56**, 8798–8801.

30 G. A. Monti, N. M. Correa, R. D. Falcone, G. F. Silbestri and F. Moyano, *RSC Adv.*, 2020, **10**, 15065–15071.

31 J. Herranz, J. Durst, E. Fabbri, A. Patru, X. Cheng, A. A. Permyakova and T. J. Schmidt, *Nano Energy*, 2016, **29**, 4–28.

32 E. Meloni, M. Martino and V. Palma, *Catalysts*, 2020, **10**, 352–389.

33 N. Pittayaporn, A. Therdthianwong and S. Therdthianwong, *J. Appl. Electrochem.*, 2018, **48**, 251–262.

34 A. V. Chistyakov, P. A. Zharova, M. V. Tsodikov, S. A. Nikolaev, I. N. Krotova and D. I. Ezzhelenko, *Kinet. Catal.*, 2016, **57**, 803–811.

35 A. Hatamie, E. Rezvani, A. S. Rasouli and A. Simchi, *Electroanalysis*, 2018, **30**, 504–511.

36 Y. Wang and P. B. Balbuena, *J. Phys. Chem. B*, 2005, **109**, 18902–18906.

37 D. T. Thompson, *Nano Today*, 2007, **2**, 40–43.

38 Z. Yang, D. J. Lichtenwalner, A. S. Morris, J. Krim and A. I. Kingon, *J. Microelectromech. Syst.*, 2009, **18**, 287–295.

39 S. John, *An Analysis of Nickel Price Variation and its Impact on the Global Economy*, Krakow, 2015.

40 R. Du, W. Jin, H. Wu, R. Hübner, L. Zhou, G. Xue, Y. Hu and A. Eychmüller, *J. Mater. Chem. A*, 2021, **9**, 17189–17197.

41 C. Zhu, Q. Shi, S. Fu, J. Song, D. Du, D. Su, M. H. Engelhard and Y. Lin, *J. Mater. Chem. A*, 2018, **6**, 7517–7521.

42 R. Du, J. O. Joswig, X. Fan, R. Hübner, D. Spittel, Y. Hu and A. Eychmüller, *Matter*, 2020, **2**, 908–920.

43 R. Du, Y. Hu, R. Hübner, J. Joswig, X. Fan, K. Schneider and A. Eychmüller, *Sci. Adv.*, 2019, **5**, 4590–4598.

44 B. Cai, R. Hübner, K. Sasaki, Y. Zhang, D. Su, C. Ziegler, M. B. Vukmirovic, B. Rellinghaus, R. R. Adzic and A. Eychmüller, *Angew. Chem., Int. Ed.*, 2018, **57**, 2963–2966.

45 X. Gao, R. J. A. Esteves, L. Nahar, J. Nowaczyk and I. U. Arachchige, *ACS Appl. Mater. Interfaces*, 2016, **8**, 13076–13085.

46 Q. Shi, C. Zhu, H. Zhong, D. Su, N. Li, M. H. Engelhard, H. Xia, Q. Zhang, S. Feng, S. P. Beckman, D. Du and Y. Lin, *ACS Energy Lett.*, 2018, **3**, 2038–2044.

47 B. Cai, D. Wen, W. Liu, A.-K. Herrmann, A. Benad and A. Eychmüller, *Angew. Chem., Int. Ed.*, 2015, **54**, 13101–13105.

48 B. Cai, A. Dianat, R. Hübner, W. Liu, D. Wen, A. Benad, L. Sonntag, T. Gemming, G. Cuniberti and A. Eychmüller, *Adv. Mater.*, 2017, **29**, 1605254–1605261.

49 W. Liu, D. Haubold, B. Rutkowski, M. Oschatz, R. Hübner, M. Werheid, C. Ziegler, L. Sonntag, S. Liu, Z. Zheng, A.-K. Herrmann, D. Geiger, B. Terlan, T. Gemming, L. Borchardt, S. Kaskel, A. Czyrska-Filemonowicz and A. Eychmüller, *Chem. Mater.*, 2016, **28**, 6477–6483.

50 K. G. S. Ranmohotti, X. Gao and I. U. Arachchige, *Chem. Mater.*, 2013, **25**, 3528–3534.

51 M. Oezaslan, A.-K. Herrmann, M. Werheid, A. I. Frenkel, M. Nachtegaal, C. Dosche, C. Laugier Bonnaud, H. C. Yilmaz, L. Kühn, E. Rhiel, N. Gaponik, A. Eychmüller and T. J. Schmidt, *ChemCatChem*, 2017, **9**, 798–808.

52 M. Oezaslan, W. Liu, M. Nachtegaal, A. I. Frenkel, B. Rutkowski, M. Werheid, A. K. Herrmann, C. Laugier-Bonnaud, H. C. Yilmaz, N. Gaponik, A. Czyrska-Filemonowicz, A. Eychmüller and T. J. Schmidt, *Phys. Chem. Chem. Phys.*, 2016, **18**, 20640–20650.

53 P. Yan, E. Brown, Q. Su, J. Li, J. Wang, C. Xu, C. Zhou and D. Lin, *Small*, 2017, **13**, 1701756–1701762.

54 Y. Tang, K. L. Yeo, Y. Chen, L. W. Yap, W. Xiong and W. Cheng, *J. Mater. Chem. A*, 2013, **1**, 6723–6726.

55 H. L. Gao, L. Xu, F. Long, Z. Pan, Y. X. Du, Y. Lu, J. Ge and S. H. Yu, *Angew. Chem., Int. Ed.*, 2014, **53**, 4561–4566.

56 M. Z. Yazdan-Abad, M. Noroozifar, A. S. Douk, A. R. Modarresi-Alam and H. Saravani, *Appl. Catal., B*, 2019, **250**, 242–249.

57 Q. Shi, C. Zhu, Y. Li, H. Xia, M. H. Engelhard, S. Fu, D. Du and Y. Lin, *Chem. Mater.*, 2016, **28**, 7928–7934.

58 S. Naskar, A. Freytag, J. Deutsch, N. Wendt, P. Behrens, A. Köckritz and N. C. Bigall, *Chem. Mater.*, 2017, **21**, 9208–9217.

59 Y. Zeng, Y. Li, X. Tan, J. Gong, Z. Wang, Y. An, Z. Wang and H. Li, *Appl. Mater. Interfaces*, 2021, **13**, 36816–36823.

60 Q. Shi, C. Zhu, M. Tian, D. Su, M. Fu and M. H. Engelhard, *Nano Energy*, 2018, **53**, 1–22.

61 A. A. Dubale, Y. Zheng, H. Wang, R. Hübner, Y. Li, J. Yang, J. Zhang, N. K. Sethi, L. He, Z. Zheng and W. Liu, *Angew. Chem., Int. Ed.*, 2020, **59**, 13891–13899.

62 H. Wang, L. Jiao, L. Zheng, Q. Fang, X. Qin, X. Luo, X. Wei, L. Hu, W. Gu, J. Wen and C. Zhu, *Adv. Funct. Mater.*, 2021, **31**, 2103465.

63 D. Wenchao, P. Zhang, Y. Xiahou, Y. Song, C. Bi, J. Zhan, W. Du, L. Huang, H. Möhwald and H. Xia, *Appl. Mater. Interfaces*, 2018, **10**, 23081–23093.

64 C. Wang, W. Duan, L. Xing, Y. Xiahou, W. Du and H. Xia, *J. Mater. Chem. B*, 2019, **7**, 7588–7598.

65 K. Hiekel, S. Jungblut, M. Georgi and A. Eychmüller, *Angew. Chem., Int. Ed.*, 2020, **59**, 12048–12054.

66 C. Wang, J. Herranz, R. Hübner, T. J. Schmidt and A. Eychmüller, *Acc. Chem. Res.*, 2023, **56**, 237–247.

67 W. Liu, P. Rodriguez, L. Borchardt, A. Foelske, J. Yuan, A. K. Herrmann, D. Geiger, Z. Zheng, S. Kaskel, N. Gaponik, R. Kötz, T. J. Schmidt and A. Eychmüller, *Angew. Chem., Int. Ed.*, 2013, **52**, 9849–9852.

68 A. K. Herrmann, P. Formanek, L. Borchardt, M. Klose, L. Giebeler, J. Eckert, S. Kaskel, N. Gaponik and A. Eychmüller, *Chem. Mater.*, 2014, **26**, 1074–1083.

69 M. Wang, W. Zhang, J. Wang, D. Wexler, S. D. Poynton, R. C. T. Slade, H. Liu, B. Winther-Jensen, R. Kerr, D. Shi and J. Chen, *ACS Appl. Mater. Interfaces*, 2013, **5**, 12708–12715.

70 C. Shang, W. Hong, J. Wang and E. Wang, *J. Power Sources*, 2015, **285**, 12–15.

71 D. L. Van Hyning and C. F. Zukoski, *Langmuir*, 1998, **14**, 7034–7046.

72 M. Dragan, *Catalysts*, 2022, **12**, 356–373.

73 W. P. Davey, *Phys. Rev.*, 1925, **25**, 753–761.

74 F. Matter, A. L. Luna and M. Niederberger, *Nano Today*, 2020, **30**, 100827–100847.

75 J. Sopoušek, A. Kryštofová, M. Premović, O. Zobač, S. Polsterová, P. Brož and J. Buršík, *Calphad Comput. Coupling Phase Diagrams Thermochem.*, 2017, **58**, 25–33.

76 P. P. Fedorov and S. N. Volkov, *Russ. J. Inorg. Chem.*, 2016, **61**, 772–775.

77 M. Georgi, J. Kresse, K. Hiekel, R. Hübner and A. Eychmüller, *Catalysts*, 2022, **12**, 441–452.

78 M. Mohsen-Nia, H. Amiri and B. Jazi, *J. Solution Chem.*, 2010, **39**, 701–708.

79 G. Åkerlöf, *J. Am. Chem. Soc.*, 1932, **54**, 4125–4139.

80 F. Hofmeister, *Arch. Exp. Pathol. Pharmakol.*, 1888, **24**, 247–260.

81 V. Mazzini and V. S. J. Craig, *Chem. Sci.*, 2017, **8**, 7052–7065.

82 M. Thommes, K. Kaneko, A. V. Neimark, J. P. Olivier, F. Rodriguez-Reinoso, J. Rouquerol and K. S. W. Sing, *Pure Appl. Chem.*, 2015, **87**, 1051–1069.

83 G. Reichenauer and G. W. Scherer, *J. Non-Cryst. Solids*, 2001, **285**, 167–174.

84 G. Reichenauer and G. W. Scherer, *J. Colloid Interface Sci.*, 2001, **236**, 385–386.

85 H. Wang, Y. Cao, J. Li, J. Yu, H. Gao, Y. Zhao, Y. Kwon and G. Li, *Ionics*, 2018, **24**, 2745–2752.

86 W. Jud, C. A. Salazar, J. Imbrogno, J. Verghese, S. M. Guinness, J. N. Desrosiers, C. O. Kappe and D. Cantillo, *Org. Process Res. Dev.*, 2022, **26**, 1486–1495.

87 L. Wang, W. Zhu, W. Lu, L. Shi, R. Wang, R. Pang, Y. Y. Cao, F. Wang and X. Xu, *Biosens. Bioelectron.*, 2019, **142**, 111577.

88 Z. Yan, Z. Xu and S. Yang, *Adv. Mater. Res.*, 2012, **345**, 60–65.

89 T. Taghvaee, S. Donthula, P. M. Rewatkar, H. Majedi Far, C. Sotiriou-Leventis and N. Leventis, *ACS Nano*, 2019, **13**, 3677–3690.